PHYSICAL REVIEW FLUIDS **9**, 044801 (2024)

Experimental study of the turbulence ingestion noise of rotor blades

Han Wu, Yuhong Li, and Xin Zhang*
Department of Mechanical and Aerospace Engineering, The Hong Kong University of Science and Technology, Clear Water Bay, Kowloon, Hong Kong SAR, China

Siyang Zhong
Department of Aeronautical and Aviation Engineering, The Hong Kong Polytechnic University, Hung Hom, Kowloon, Hong Kong SAR, China

Xun Huang†
State Key Laboratory of Turbulence and Complex Systems, Department of Aeronautics and Astronautics, College of Engineering, Peking University, Beijing 100871, China

(Received 1 November 2023; accepted 19 March 2024; published 9 April 2024)

The ingestion of turbulence can cause additional noise sources of rotor blades, which should be considered for multirotor powered urban air mobility vehicles encountering atmospheric turbulence. In this work, a turbulence grid was installed in the exit of an open-jet anechoic wind tunnel to generate turbulent flows. The grid turbulence was characterized using hot-wire anemometry, showing that turbulence intensity decays with the streamwise locations downstream of the grid, following a power law of $-5/7$. The power spectral properties of the grid turbulence were also assessed, and it agrees well with the von Kármán turbulence spectrum in the inertial subrange. Then, the aerodynamic force and noise of a rotor with a diameter of 217.2 mm were measured under both clean and turbulent flows. Force measurements show that the thrust and torque coefficients decrease with the advance ratio J. Noise measurements show that the tonal noise at the blade pass frequency (BPF) is more significant at the upstream locations under high advance ratios, and high-order BPF harmonics can also be amplified. Moreover, the turbulence ingestion noise mainly dominates the broadband contents from 10 to 50 BPF harmonics. The broadband noise can be scaled by the Mach number scaling of $M_\infty^2 M_c^4$, where M_∞ is the freestream Mach number and M_c is the corresponding Mach number of the rotating speed at the blade tip.

DOI: 10.1103/PhysRevFluids.9.044801

I. INTRODUCTION

Multirotor configurations are increasingly employed in novel flying vehicles operating in urban areas. The rotors are often powered electrically to reduce carbon footprints [1,2], which leaves the inevitable noise pollution as the major environmental concern. The rotor noise is the main noise source, primarily caused by the unsteady flows around the blades. The blades generate discrete tonal components mainly at the blade pass frequency (BPF) and its harmonics, as well as broadband noise mainly caused by the turbulent flows [3]. A recent study by Zhong *et al.* [4] suggests that the random fluctuations of the rotating speed or vibration may also contribute to the broadband-type noise generation.

*aexzhang@ust.hk
†huangxun@pku.edu.cn

Rotor noise has been a long-standing research topic since the last century [5,6]. In recent years, the developments of multirotor powered unmanned aircraft systems (UASs), including small-scale drones and urban air mobility (UAM) vehicles, have renewed research interest in rotor noise. Compared to conventional helicopter rotors, the tip Mach number and Reynolds number of rotor blades for UAS vehicles are relatively low [7–9]. Hence, continuous efforts are still being made to understand the rotor noise characteristics in different flow conditions that mimic various vehicle flight states [10–15]. In practical applications, the UAS vehicles can also be subjected to ambient turbulence during operations [16,17], which, however, has not resulted in sufficient studies in the past. Thus, understanding the effects of turbulence ingestion on the aerodynamics and acoustics of a rotor is substantial for the noise control strategy for UAS.

The ingestion of turbulence can lead to unsteady loadings on the rotor blades, generating sound that can be radiated to the far field. In pioneering experimental studies, the oncoming turbulence was often assumed homogeneous and isotropic [18]. Sevik [18] investigated the unsteady thrust of a ten-bladed rotor fully immersed in grid-generated turbulence. A theoretical model for predicting rotor unsteady thrust was given as an aerodynamic response function based on the Sears theory [19]. "Humps" or "haystacks" around BPF harmonics were observed in the experiments. Although Sevik's model [18] could get good agreement with the measurements in broadband sound, it failed to predict the tonal components at BPF harmonics. To characterize the aeroacoustic response of rotors, Wojno *et al.* [20,21] measured the ingested velocity field and resulting far-field noise. The turbulence characteristics were combined with a blade response function to estimate the far-field acoustic spectral properties. They suggested that the blade-to-blade correlation should be considered for predicting the BPF harmonics. Recently, Wu *et al.* [22] numerically studied a rotor ingesting grid turbulence, where the inflow turbulence caused by the grid was directly simulated. Their results highlighted that the unsteady thrust due to turbulence ingestion was the main contributor to the far-field noise, and the multiple cutting of consecutive rotor blades with coherent vortical structures was the main interaction.

Modern propulsion systems, such as marine propellers or aircraft engines, are often integrated into the ship or airframe. The rotor blades can ingest large-scale vortical structures induced by upstream bodies during operations, such as boundary layers of the engine inlet or the turbulent wake of the hull. Glegg *et al.* [23–26] investigated the acoustic properties of a propeller ingesting planar boundary layers under various thrusting conditions. Velocity correlations can be measured by hot-wire probes installed at the blade leading edge, which were used to describe the inflow statistics and reveal the correlations of multiple blades when vortex structures were ingested [23,25]. The rotor generated tonal noise haystacks by ingesting boundary layers, while significant tonal features can be found at high thrusting conditions due to highly correlated blade-vortex interactions. The noise features produced by interactions of rotor and turbulence could vary with different thrusting conditions, suggesting that a comprehensive test matrix should be considered for investigating the turbulence ingestion noise of rotors [26].

Unlike marine propeller and aircraft engine fans, rotors of UAS vehicles could possibly be subjected to atmospheric turbulence [16]. In experiments, small-scale turbulence is often generated by means of a grid to simulate the atmospheric flow conditions. Hagen *et al.* [27] investigated the effect of ingesting atmospheric turbulence into an isolated tail rotor, with turbulence intensity controlled by the types of the passive grid. Results showed that the broadband floor raised across the whole spectrum. Studies on small-scale propellers have shown that ingesting turbulent inflow in confined anechoic chambers can increase broadband noise level [28,29]. The ingested turbulent inflow was caused by the rotor wake recirculation inside the test section, which was not well prescribed. Wind tunnel measurements were performed to study the aeroacoustic characteristics of rotors immersed in grid turbulence or turbulent wake of an airfoil [30–34], among others. Jamaluddin *et al.* [34] experimentally studied the turbulence ingestion noise of a rotor operating at a constant rotational speed, suggesting high-frequency broadband noise could also be increased by turbulent inflow, especially at higher advance ratios.

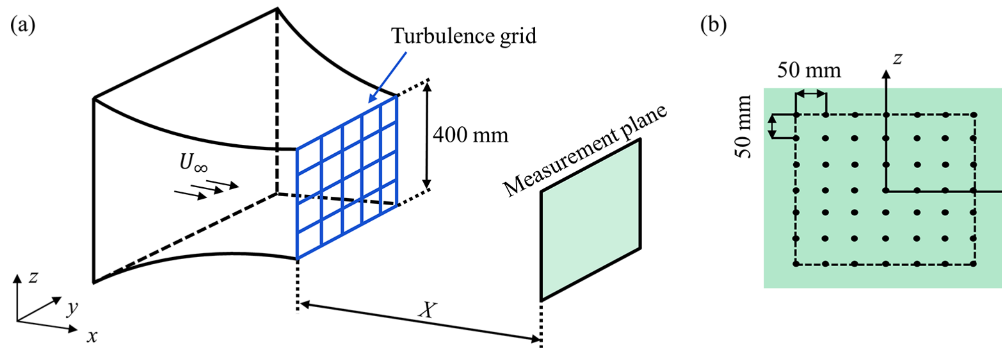

FIG. 1. Schematic of the turbulence measurement: (a) the jet nozzle with turbulence grid installed; (b) measured points on each measurement plane.

In general, rotors of UAS are commonly operating at a higher rotational speed with fewer blades [10,34,35], compared to the underwater propellers [18,22,26]. In addition, flow transitions can exist on the blade surface. The surface flow can be separated at high advance ratios, which causes generations of broadband noise [14]. In actual operations, the UAS can be subjected to a variety of flight speeds based on the requirements of missions [36], which can lead to different thrusting conditions of the rotor and also different noise features.

This study aims at understanding the influence of turbulent inflows on rotor noise under various thrusting states. A passive turbulence grid is implemented to simulate atmospheric turbulence. The turbulence is characterized by the hot-wire anemometry, and the rotor noise is measured in both turbulent and clean flows. A variety of rotational speeds and flow velocities are considered in this work. The resulting tonal and broadband noise contents of turbulence ingestion are analyzed, respectively.

In the remaining part of this paper, Sec. II presents the experimental setup for turbulence and noise measurements. Sections III and IV present the turbulence and noise measurement results, respectively. Section V is the conclusion.

II. EXPERIMENTAL SETUP

A. Wind tunnel facility

This study was conducted in the anechoic wind tunnel at the Hong Kong University of Science and Technology (HKUST) [37]. The wind tunnel is enclosed by an anechoic chamber of 3.3 m (length)×3.1 m (width)×2.0 m (height), with a cutoff frequency of 200 Hz. The chamber has an open-jet nozzle of 400 mm×400 mm and a jet collector to facilitate the flow. The internal structure of the collector is acoustically treated to mitigate the sound reflection.

B. Measurement setup for turbulence characterization

The turbulence grid was installed in the jet exit to generate the turbulent flow [indicated by blue in Fig. 1(a)]. A Cartesian coordinate (x, y, z) is implemented for the interpretation of the measurement. The streamwise, transverse, and vertical directions are represented by x, y, and z, respectively. The origin of the coordinate is located in the center of the jet exit. U_∞ denotes the flow velocity right before interacting with the grid. Measurements were conducted on multiple downstream planes parallel to the jet nozzle, giving 7×7 points for each measured plane as shown in Fig. 1(b). The distance downstream the grid (of the measured plane) is denoted by X.

A square-mesh type grid was implemented in the experiment. The grid has a dimension of 400 mm×400 mm, which can be characterized by the rod diameter d and the mesh length M,

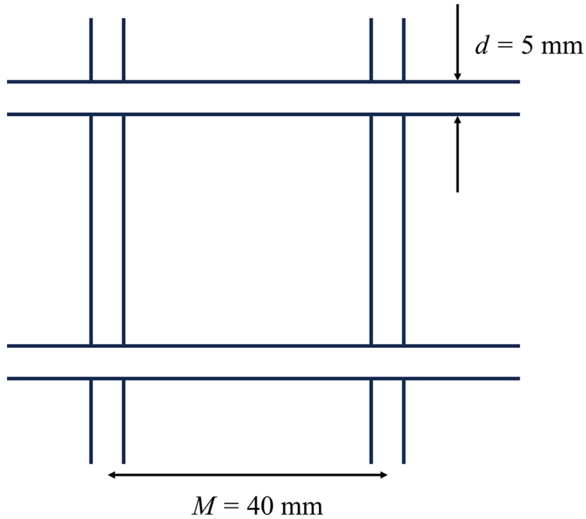

FIG. 2. The dimensions of turbulence grid: rod diameter d and mesh size M.

as shown in Fig. 2. The grid is constructed by rods in a square-mesh manner, yielding a mesh size of $M = 40$ mm. Each rod has a round cross-section with a diameter of 5 mm. The resulting porosity $\beta = (1 - d/M)^2$ of the turbulence grid is 0.765. The grid was manufactured by computer numeric control machining from an aluminum sheet with a thickness of 5 mm. A photography of the installed turbulence grid is shown in Fig. 3(a).

C. Hot-wire anemometry

The velocity profile and turbulence properties of the incoming flow were characterized by the hot-wire anemometry, with a Dantec type 55P11 single-wire probe and a type 55P61 two-component cross-wire probe. The single-wire probe was used for measuring the streamwise component u of the flow, while the cross-wire probe was employed to measure velocity fluctuations in both the streamwise (x) and transverse (y) velocity components simultaneously. The orientation of the probe was aligned with the x axis, supported by a metal strut as shown in Fig. 3(a). The schematic of different hot-wire probes can be referred to in Fig. 3(b). A two-dimensional Dantec transverse system with a positional accuracy of 6.25 μm was used to position the probe in the test section. The tests were conducted when the rotor was inactivated, by neglecting its potential suction effect

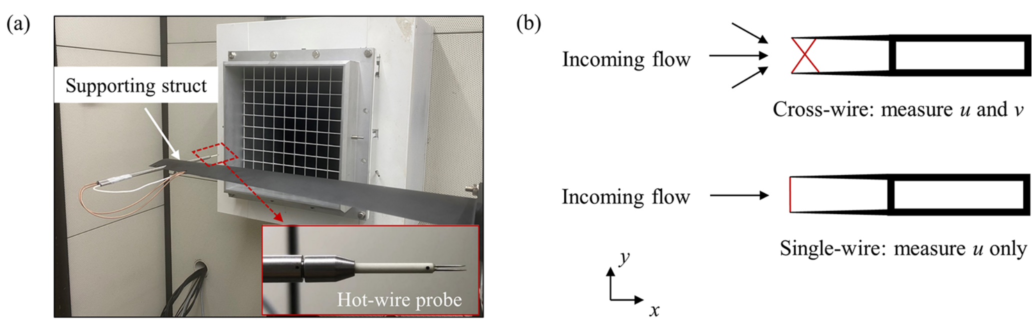

FIG. 3. The hot-wire anemometry: (a) a photo of the hot-wire measurement setup and (b) sketches of the cross-wire probe and the single-wire probe.

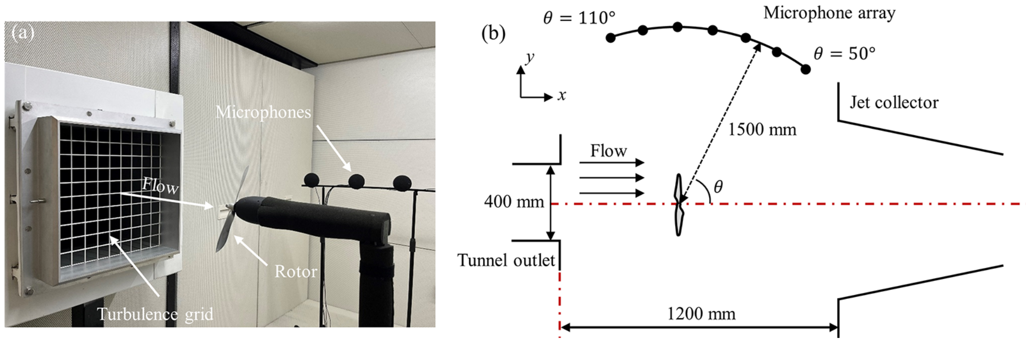

FIG. 4. Schematic of the noise measurement: (a) a photo of the rotor interacting with grid turbulence; (b) top view (not to scale).

on the ingested turbulence. The data were sampled at a rate of 20 kHz for 10 s in each measurement. For spectral analysis, the data were divided to 100 blocks with an overlapping rate of 50%. Each block containing 4000 data points was processed with a Hanning window function, leading to a frequency resolution of 5 Hz.

D. Measurement setup for turbulence-ingesting rotor noise

The custom-designed 2-bladed rotor SP2 [35] was studied using an established rotor aeroacoustic test rig [38]. The rotor has a radius of 108.6 mm. All the metallic components of the test rig were covered by sound-absorbing foam to minimize the sound reflection during experiments. For aeroacoustic measurements, testing objects are often installed within one hydraulic diameter of the jet nozzle to stay within the potential core of the jet and avoid interacting with shear layers [39]. To this end, the rotor was mounted at a distance of 400 mm to the nozzle for the current configuration. A detailed discussion of the potential core radius at the rotor plane can be found in the Appendix.

A multiaxis load cell, ATI Mini 40, was attached to the rotor system to capture blade aerodynamic loadings. The sensing range is 120 N in the direction of rotor thrust, with the resolution of $1/50$ N. For the torque, the sensing range is 2 N m with a resolution of $1/4000$ N m. The sampling frequency for the aerodynamic force and torque was 20 kHz. The rotor noise was measured by 7 G.R.A.S. type 46BE free-field microphones. The microphones were installed evenly in an arc array, at a distance of 1.5 m from the rotor. The azimuth angle of observers is defined by θ, as shown in Fig. 4(b). The sampling frequency for noise data was 50 kHz. The sampling time for each measurement was 10 s.

To obtain the acoustic spectra, Welch's method [40] for power spectral density (PSD) estimation was used. The time-series data were divided into 100 data blocks with a 50% overlap. Each block consisting of 10 000 data points was filtered by a Hanning window function, leading to a frequency resolution of 5 Hz. The sound pressure level (SPL) was computed as

$$\mathrm{SPL} = 10\log_{10}\left(\frac{\Phi_{pp}(f)\Delta f}{p_{\mathrm{ref}}^2}\right),$$

where $p_{\mathrm{ref}} = 2\times10^{-5}$ Pa, $\Phi_{pp}(f)$ is the power spectral density of the far-field sound pressure, and Δf is the frequency resolution.

III. CHARACTERISTICS OF THE GRID TURBULENCE

In this section, the characteristics of the grid generated turbulence are discussed. First, the homogeneity of grid turbulence is presented. Second, turbulence intensities are measured along several streamwise locations to demonstrate the evolution of the grid turbulence. Then, we assess the isotropy of the turbulence by comparing the integral length scales of the streamwise and transverse

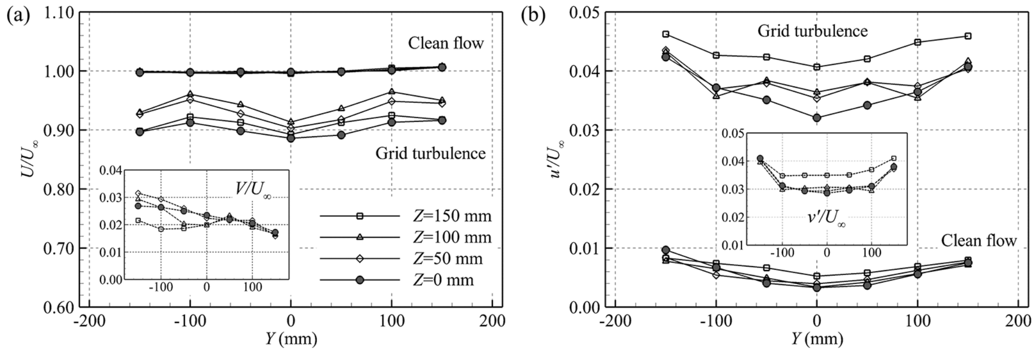

FIG. 5. Flow homogeneity at $U_\infty = 10$ m/s: (a) mean velocity U (symbols with solid lines) and V (inset, symbols with dashed lines); (b) velocity fluctuations u' (symbols with solid lines) and v' (inset, symbols with dashed lines). All the data were acquired at $X/d = 97.8$, and they were normalized by U_∞.

flows. The spectral properties of the grid turbulence are also discussed. Finally, we evaluate the turbulence Gaussianity to reveal the deviation from fully isotropic turbulence.

A. Flow homogeneity

Figures 5 and 6 present normalized mean velocities (U, V) and the root-mean-square of the velocity fluctuations, u' (streamwise) and v' (transverse) at $U_\infty = 10$ and 15 m/s. The results along different locations on the measurement plane are compared to assess the flow homogeneity. In this study, the flow homogeneity is regarded as high if the spatial variations of the flow variables are small, and vice versa. For the streamwise mean flow component U, the clean flow without turbulence grid is employed as a baseline configuration for comparison. As shown in Figs. 5(a) and 6(a), the clean flow results demonstrate good uniformity across the vertical direction z, whereas significant discrepancies are observed for the cases with turbulence grid. Moreover, the streamwise velocity is reduced due to the interaction with grids. For the transverse component V, an increasing pattern towards the negative y-direction is observed from the velocity profiles.

For the velocity fluctuations, both u' and v' are symmetrical with respect to the z-axis. The amplitude of u' is slightly larger than v' for both figures. The values of u' for grid turbulence are compared to clean flow cases, suggesting a considerable increase in velocity fluctuations caused by the grid. In particular, the grid turbulence shows remarkable discrepancies along the Z-axis. Notably, the deviations in the transverse profiles of v' are less significant. Overall, the velocity profiles in Figs. 5 and 6 exhibit similar patterns.

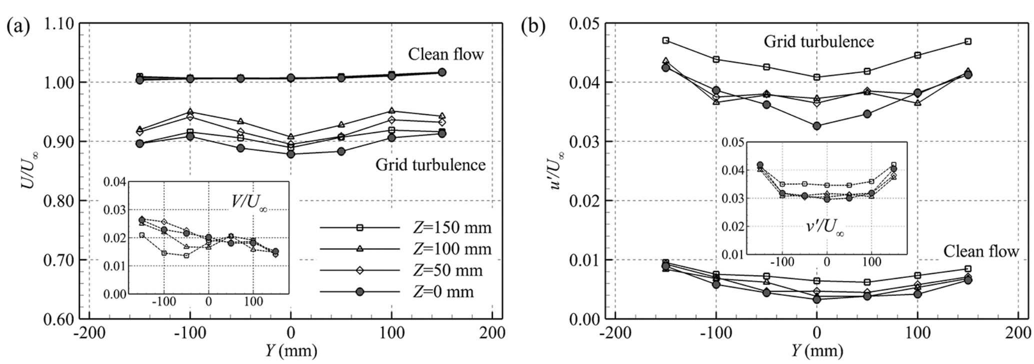

FIG. 6. Flow homogeneity at $U_\infty = 15$ m/s. Others are the same as those in Fig. 5.

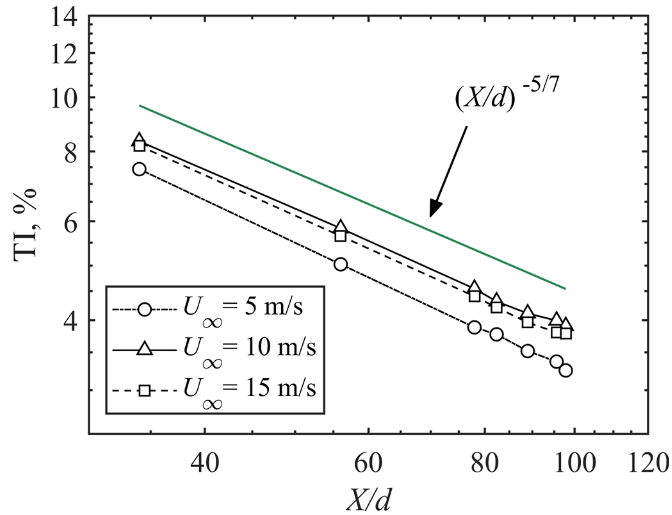

FIG. 7. Streamwise turbulence intensity profiles measured at the wind tunnel center vs X/d. The results show a decay power law of $-5/7$ for nearly isotropic grid turbulence [42].

B. Decay of turbulence intensity in streamwise direction

The streamwise turbulence intensity (TI) is defined by

$$\mathrm{TI} = \frac{u'}{U}, \tag{1}$$

where u' and U are the velocity fluctuation and the mean velocity, respectively. Figure 7 shows the evolution of TI of the streamwise component, which is measured by the single-wire probe, for $U_\infty = 5$, 10, and 15 m/s. The streamwise evolution of turbulence exhibits a similar decay trend for all the measured cases, with a decay power law of $(X/d)^{-5/7}$. This trend is in agreement with theoretical analyses of isotropic turbulence by Frenkel [41] and experimental data from square-mesh grids of round rods [42]. The decay of the grid turbulence can affect aeroacoustic as it influences the strengths of the unsteady loading on the rotor blade.

C. Turbulence isotropy

In this section, we assess turbulence isotropy through different approaches. First, the power spectral characteristics are analyzed. Then, the large-scale isotropy of the grid turbulence is also investigated using the u' and v' results measured by the X-wire probe.

1. Power spectral properties

The power spectral density of grid turbulence, $E_{uu}(f)$, is often compared to the von Kármán spectrum [43], which implicitly assumes the turbulence as isotropic. The von Kármán spectrum, denoted by $E_{uu}^{(*)}(f)$, is expressed in one-dimensional form as

$$E_{uu}^{(*)}(f) = \frac{4u'^2 L_{uu}}{U} \frac{1}{\left[1 + (k_x/k_e)^2\right]^{5/6}}, \tag{2}$$

where

$$\frac{k_x}{k_e} = 2\sqrt{\pi}\frac{\Gamma(1/3)}{\Gamma(5/6)}\frac{f L_{uu}}{U}. \tag{3}$$

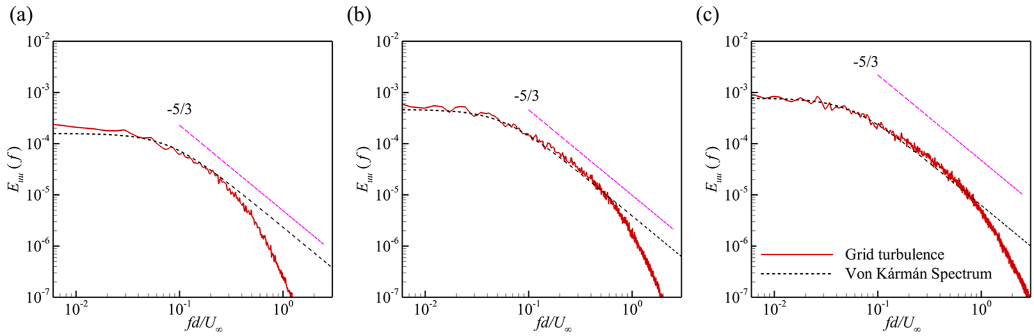

FIG. 8. Comparison of the power spectra of grid turbulence and von Kármán model for isotropic turbulence at (a) $U_\infty = 5$ m/s, (b) $U_\infty = 10$ m/s, and (c) $U_\infty = 15$ m/s.

f is the frequency, L_{uu} is the integral length scale in the streamwise direction, and Γ is the gamma function. In practice, the integral length scale L_{uu} is often estimated by extrapolating the low-frequency range of the measured power spectrum [42]

$$L_{uu} = \left[\frac{E_{uu}(f)U}{4u'^2}\right]_{f\to 0}. \tag{4}$$

In a similar manner, the transverse integral length scale, L_{vv}, can be determined by

$$L_{vv} = \left[\frac{E_{vv}(f)U}{4v'^2}\right]_{f\to 0}. \tag{5}$$

Figure 8 shows the $E_{uu}(f)$ of the streamwise velocity fluctuation, at $U_\infty = 5$, 10, and 15 m/s, respectively. The von Kármán spectrum, $E_{uu}^{(*)}(f)$, is also plotted for comparison, where L_{uu} is computed based on the hot-wire measured results by Eq. (4). The frequency is shown in the normalized form of fd/U_∞. The turbulence spectra under various U_∞ show similar spectral characteristics, which can be divided into two distinct ranges: the energy-containing range ($fd/U_\infty < 0.1$) and the equilibrium range ($fd/U_\infty > 0.1$). In the energy-containing range, vortex structures contain the majority of the energy, with their size characterized by L_{uu}. Overall, the von Kármán model underestimates the spectra levels in this range slightly, and it exhibits the expected $-5/3$ power law of energy decay over the entire equilibrium range. In general, the spectrum of grid turbulence shows good agreement with the von Kármán model. At higher frequencies, the spectrum of the grid turbulence deviates from the presumed von Kármán spectrum as the actual turbulence is within the dissipation range. Notably, the frequency where the grid turbulence starts to dissipate increases with the freestream velocity U_∞, which is expected to affect the resulting interaction noise with the downstream rotor blades.

2. Large-scale isotropy

In this work, we also investigate the large-scale isotropy of the grid turbulence using the measured u' and v' results. The streamwise evolution of the isotropy ratio u'/v', which should be 1 for the ideal isotropic turbulence, is shown in Fig. 9. For the measured cases, the value of u'/v' is generally larger than 1, and it increases with the streamwise location X. The ratio gradually converges to $u'/v' = 1.12$, which is reasonably consistent with previously reported turbulence measurements [44].

The integral length scale is a measure of the largest vortex size in the turbulent flow. For isotropic turbulence, the relationship between the streamwise and transverse integral length scales should be $L_{uu} = 2L_{vv}$ [42,45]. Figure 10 presents the streamwise profile of L_{uu} and L_{vv} measured at $U_\infty = 10$ and 15 m/s, with detailed values given in Table I. The measurements are shown in symbols, along

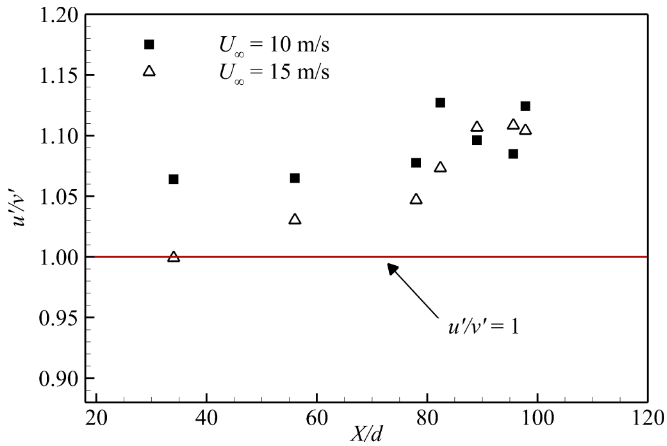

FIG. 9. Isotropy ratios, u'/v', in the streamwise direction of the grid turbulence. The data were acquired by the cross-wire probe at the center of the jet exit.

with fitted curves. The results indicate that L_{uu}/L_{vv} values are above 2 for all the measured locations, suggesting that the velocity fluctuations in the streamwise direction are more significant in the grid turbulence. The results are also consistent with the fact that the isotropy ratio u'/v' is slightly larger than 1. Moreover, the value of L_{uu}/L_{vv} appears to increase with U_∞. Both L_{uu} and L_{vv} increase with the streamwise location X following a power law of 1/2, which is consistent with previous works on nearly isotropic turbulence [42,46–49].

D. Gaussianity

The Gaussianity of grid turbulence is assessed using the probability density function (PDF) of the time series of velocity fluctuations, $u'(t)$, to indicate the velocity skewness [50–52]. For the ideal isotropic turbulence, the PDF is expected to be Gaussian. The results at freestream velocities of $U_\infty = 10$ and 15 m/s are depicted in Fig. 11. Ideal Gaussian PDF curves with the same deviations are also shown for comparison. The results indicate that the data from the present study follow a Gaussian distribution regardless of freestream velocity. This suggests that there is no discernible directional trend in the turbulent fluctuations.

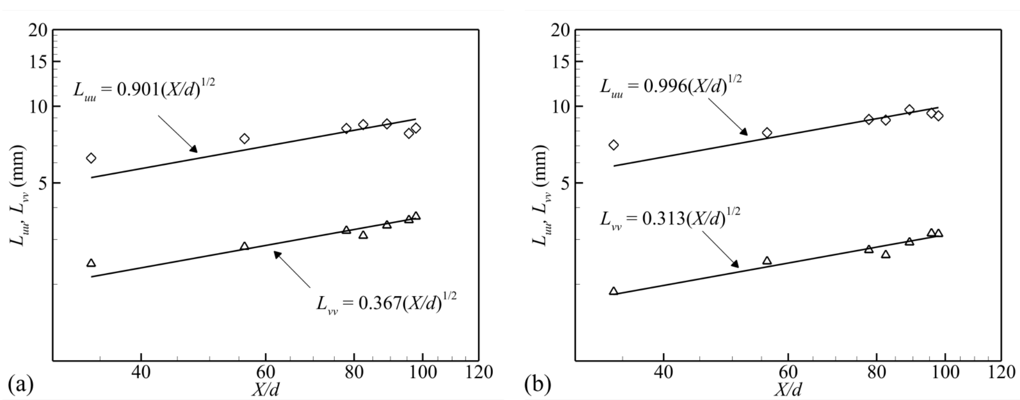

FIG. 10. Streamwise integral length scale profiles of both L_{uu} and L_{vv}: (a) $U_\infty = 10$ m/s and (b) $U_\infty = 15$ m/s. The data were acquired by the cross-wire probe at the center of the jet exit.

TABLE I. Integral length scales at various streamwise locations for $U_\infty = 10$ and 15 m/s.

X/d	$U_\infty = 10$ m/s		$U_\infty = 15$ m/s	
	L_{uu} (mm)	L_{vv} (mm)	L_{uu} (mm)	L_{vv} (mm)
34.0	6.26	2.41	7.05	1.87
56.0	7.46	2.81	7.88	2.46
78.0	8.18	3.25	8.88	2.73
82.4	8.47	3.11	8.83	2.61
89.0	8.53	3.41	9.69	2.92
95.6	7.82	3.57	9.40	3.17
97.8	8.21	3.69	9.17	3.16

We also calculated the PDF functions of the time derivative of $u'(t)$, which provides information on the intermittency of small-scale turbulence motions [53]. Figure 12 presents the $\partial u'(t)/\partial t$ results normalized by their root-mean-square values. While the $\partial u'(t)/\partial t$ results do not fit the Gaussian curves, they share similar patterns at both $U_\infty = 10$ and 15 m/s, indicating more active small-scale turbulence motion in the positive flow direction. These findings suggest a non-Gaussian behavior in the small-scale turbulence motion, which is consistent with previous studies [53].

In this section, we assess the characteristics of turbulence using various approaches. The streamwise evolutions of turbulence intensity and integral length scale show that the turbulence is nearly isotropic. The turbulence power spectral density is analyzed, suggesting that the turbulence deviates from the ideal von Kármán spectrum at higher frequencies. The PDF of streamwise velocity fluctuations and their time derivatives are calculated to see the large- and small-scale intermittency. The u' shows a Gaussian statistical behavior, while the small-scale intermittency can be demonstrated by the PDF of $\partial u'/\partial t$, indicating a tendency towards the positive flow direction.

IV. AERODYNAMIC AND AEROACOUSTIC MEASUREMENTS FOR THE ROTOR-GRID TURBULENCE INTERACTION

A. Force measurement

In this study, a rotor was tested at different rotational speeds of 90, 100, 110, and 120 revolutions per second (RPS) under various freestream velocities U_∞. The advance ratio is defined as

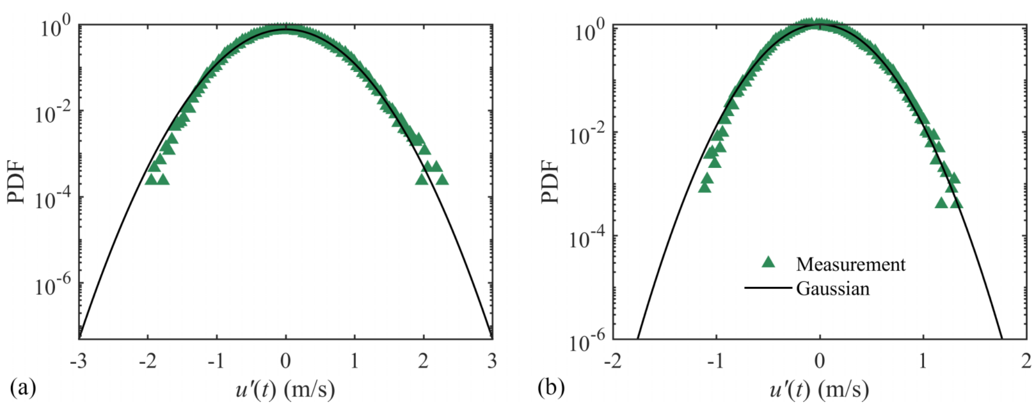

FIG. 11. Probability density function of the streamwise velocity fluctuations u' at (a) $U_\infty = 10$ m/s and (b) $U_\infty = 15$ m/s. The data were acquired by the single-wire probe at the center of the measured plane at $X/d = 77.8$.

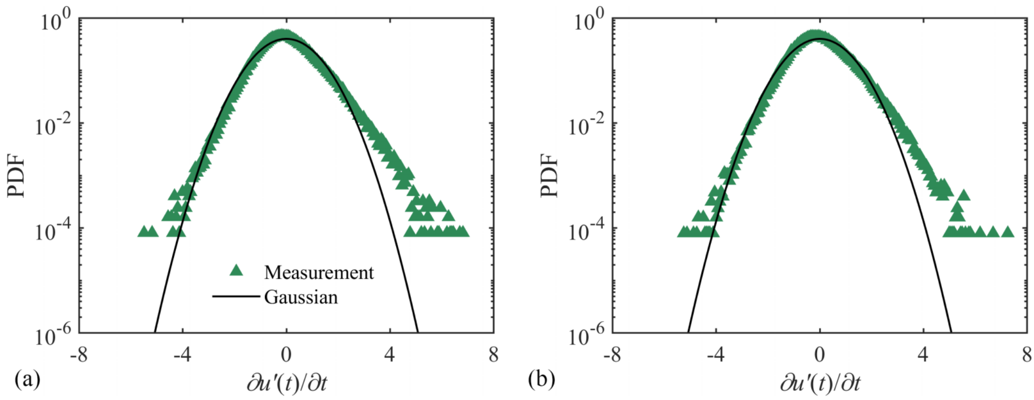

FIG. 12. Probability density function of the time derivatives of streamwise velocity fluctuations, $\partial u'/\partial t$, at (a) $U_\infty = 10$ m/s and (b) $U_\infty = 15$ m/s. The data were acquired by the single-wire probe at the center of the measured plane at $X/d = 77.8$. The values of $\partial u'/\partial t$ are normalized by their rms values.

$J = U_\infty/(nD)$, where n is the rotor rotational speeds in RPS, and D denotes the rotor diameter. The averaged thrust T and torque Q are computed based on the sampling history of the load sensor. Repeatability runs were conducted to quantify the uncertainties of load measurement. The calculation method can be referred to in [15]. The measurement uncertainties for T and Q are 0.09 N and 0.87 N mm, respectively. Time-averaged values of T and Q under various advance ratios and rotational speeds are plotted in Fig. 13, with the data obtained under clean flow and grid turbulence indicated by colored scatters. Additionally, two approximate surfaces containing all working points are also included, showing different aerodynamic performances between the two flow conditions.

Overall, for all the rotational speeds, the rotor thrust and torque decrease with the advance ratio J, as the axial freestream velocity reduces the induced velocity of the rotor disk, thus the blade loading [54]. Furthermore, it is observed that T and Q increase with n for the fixed J. For a rotor under clean flow, the blade loadings decrease more significantly compared to the rotor under grid turbulence, particularly when $J > 0.4$. This trend is mainly attributed to the fact that the axial flow velocity U of grid turbulence is smaller than 1, according to the mean flow measurements shown in Figs. 5 and 6. The transverse component V is negligible compared to U, the effect of which is thus not considered in the aerodynamic analysis. Notably, the rotor generates no thrust at the advance ratio of $J \approx 0.84$.

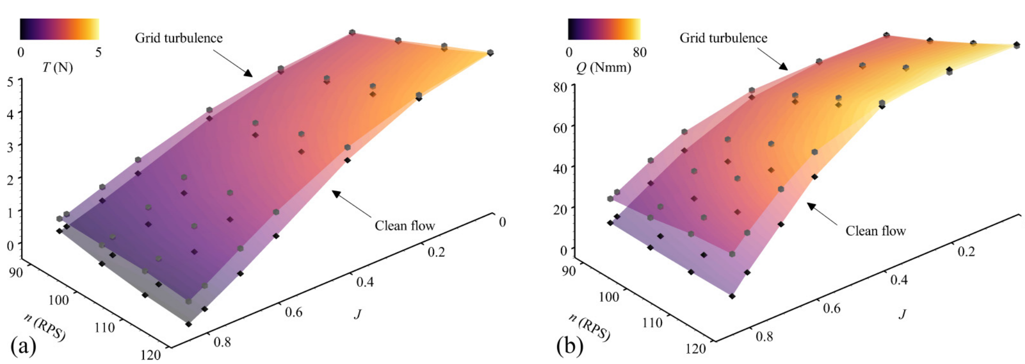

FIG. 13. Force measurement results of (a) thrust and (b) torque. Measurement points are indicated by black and gray scatters for clean flow and grid turbulence, respectively.

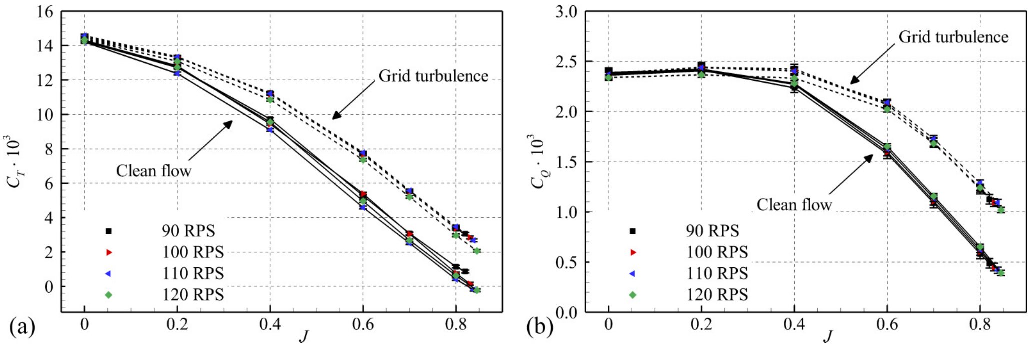

FIG. 14. Nondimensionalized force measurement results of (a) C_T and (b) C_Q.

To normalize the rotor aerodynamic performances, nondimensional thrust coefficient C_T and torque coefficient C_Q are implemented [54]:

$$C_T = \frac{T}{\rho A(\Omega R)^2}, \quad C_Q = \frac{Q}{\rho A(\Omega R)^2 R}, \tag{6}$$

where $\Omega = 2\pi n$ is the angular frequency in radians per second, ρ is the air density, A is the rotor disk area, and R is the blade radius. The results for C_T and C_Q are presented in Fig. 14, with the measurement uncertainties indicated by error bars. The C_T and C_Q curves for all rotational speeds collapse reasonably well, indicating the aerodynamic performances remain relatively stable for the tested rotational speeds. The normalized curves also exhibit a clear barrier at $J = 0.4$, dividing the current rotor thrusting into the high-thrusting region ($J < 0.4$) and low-thrusting region ($J > 0.4$). The C_T and C_Q curves drop more rapidly in the low-thrusting region.

B. Noise measurement

1. Spectral characteristics

Figure 15 presents noise spectra comparisons of turbulence-ingesting rotor noise at various advance ratios to demonstrate different spectral characteristics under high-thrusting, low-thrusting, and nonthrusting conditions. The frequency, f, is normalized by the BPF. The rotor noise exhibits strong tonal components at the first 10 BPF harmonics, while broadband noise is dominant at higher frequencies ($f/\text{BPF} > 10$) for both flow conditions. The comparison of the spectra shows a high signal-to-noise ratio of the BPF harmonics and the high-frequency broadband noise. Additionally, there are observable high-frequency spikes, as indicated in Fig. 15, which are attributed to the electric motor noise [15,38,55]. One might notice that the acoustic effect of turbulence ingestion has a strong dependency on the thrusting condition, which will be discussed further below.

Figure 16 illustrates the SPL distributions below the first 10 BPF harmonics at various n and J. The left column shows the rotor tonal noise under clean flow, while the right column shows the results obtained under grid turbulence. The data were acquired from the microphone at $\theta = 90^\circ$. In the results, the background noise is excluded by subtracting the PSD from that of the total noise. The primary BPF tone decreases as the advance ratio increases, which is consistent for all tested rotational speeds. Overall, the BPF tone is higher under grid turbulence. In contrast, high-order BPF harmonics could be amplified as J increases, such as the tone at 6×BPF at 120 RPS. Additionally, no tonal noise haystacks [18,26] are observed in this study, possibly due to the relatively low correction between the two consecutive blades of the current rotor setup. Unlike large-scale vortex or boundary layer ingestion for underwater propellers [22,26], the length scale of grid turbulence generated in this work is considerably smaller than the circumferential rotor spacing ($R = 108.6$ mm), as

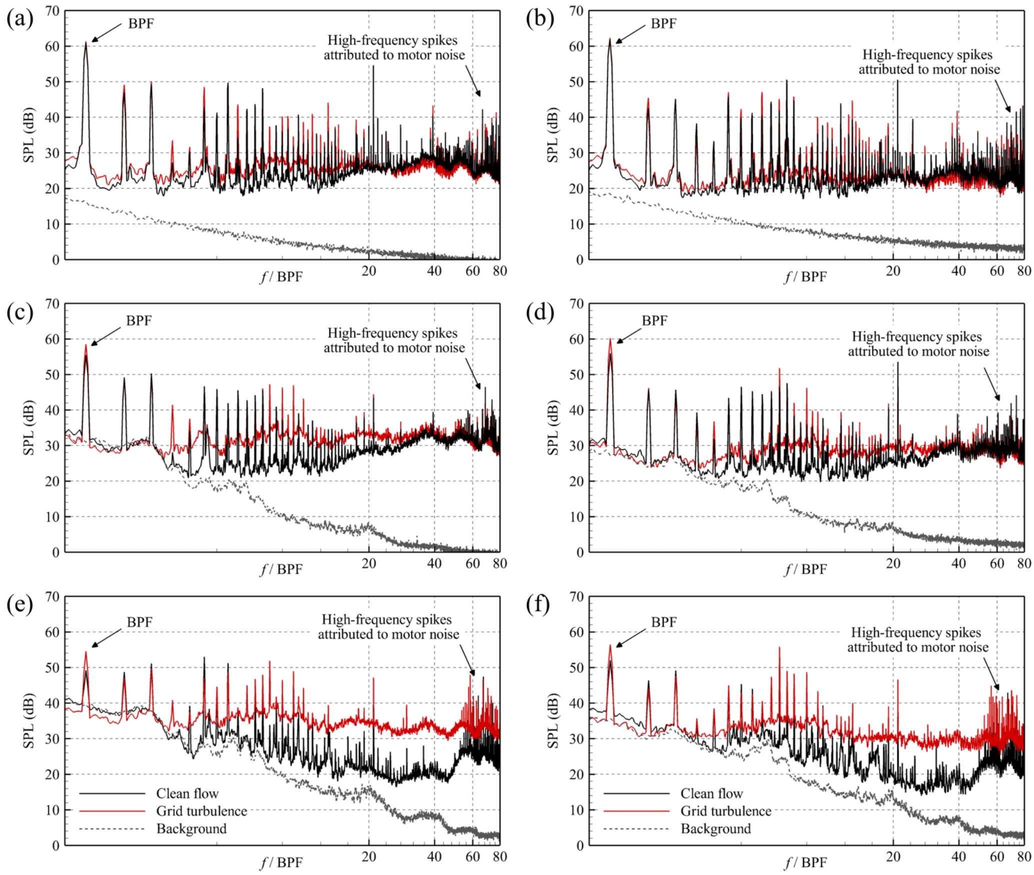

FIG. 15. SPL spectra comparison of rotor noise under various thrusting conditions at two observer angles: (a) $J = 0.2$, $\theta = 60^\circ$; (b) $J = 0.2$, $\theta = 90^\circ$; (c) $J = 0.6$, $\theta = 60^\circ$; (d) $J = 0.6$, $\theta = 90^\circ$; (e) $J = 0.84$, $\theta = 60^\circ$; (d) $J = 0.84$, $\theta = 90^\circ$. The rotation rate of the rotor is 120 RPS.

shown in Fig. 10. Thus, the bandwidth of BPF tonal noise remains consistent in the current test configuration.

Similarly, Fig. 17 shows the SPL of the broadband noise against various rotational speeds and advance ratios. The broadband contents are extracted from the narrowband spectra using a local regression method [9,55]. The frequency is normalized by the blade pass frequency. For the rotor noise under clean flow, distinguishable broadband noise can be found as the advance ratio J increases, which is attributed to trailing-edge noise [14,15]. The range of trailing-edge noise starts approximately from $f/\mathrm{BPF} = 20$, and the dominant range rises as the rotational speed increases. The noise level also increases with J and rotational speed. For turbulence ingestion noise, it mainly dominates in the low-thrusting region ($J > 0.4$). The frequency range and noise level seem to increase with the rotational speed, suggesting that the rotor-turbulence interaction is more significant. Notably, the turbulence ingestion broadband noise is considerable at $f/\mathrm{BPF} = 10$–50 compared to the clean flow configuration in the low-thrusting region. Comparisons between the two flow configurations suggest that ingested turbulence imposes a particular broadband noise source to the rotor, and the affected frequency range differs from the isolated rotor under clean flow.

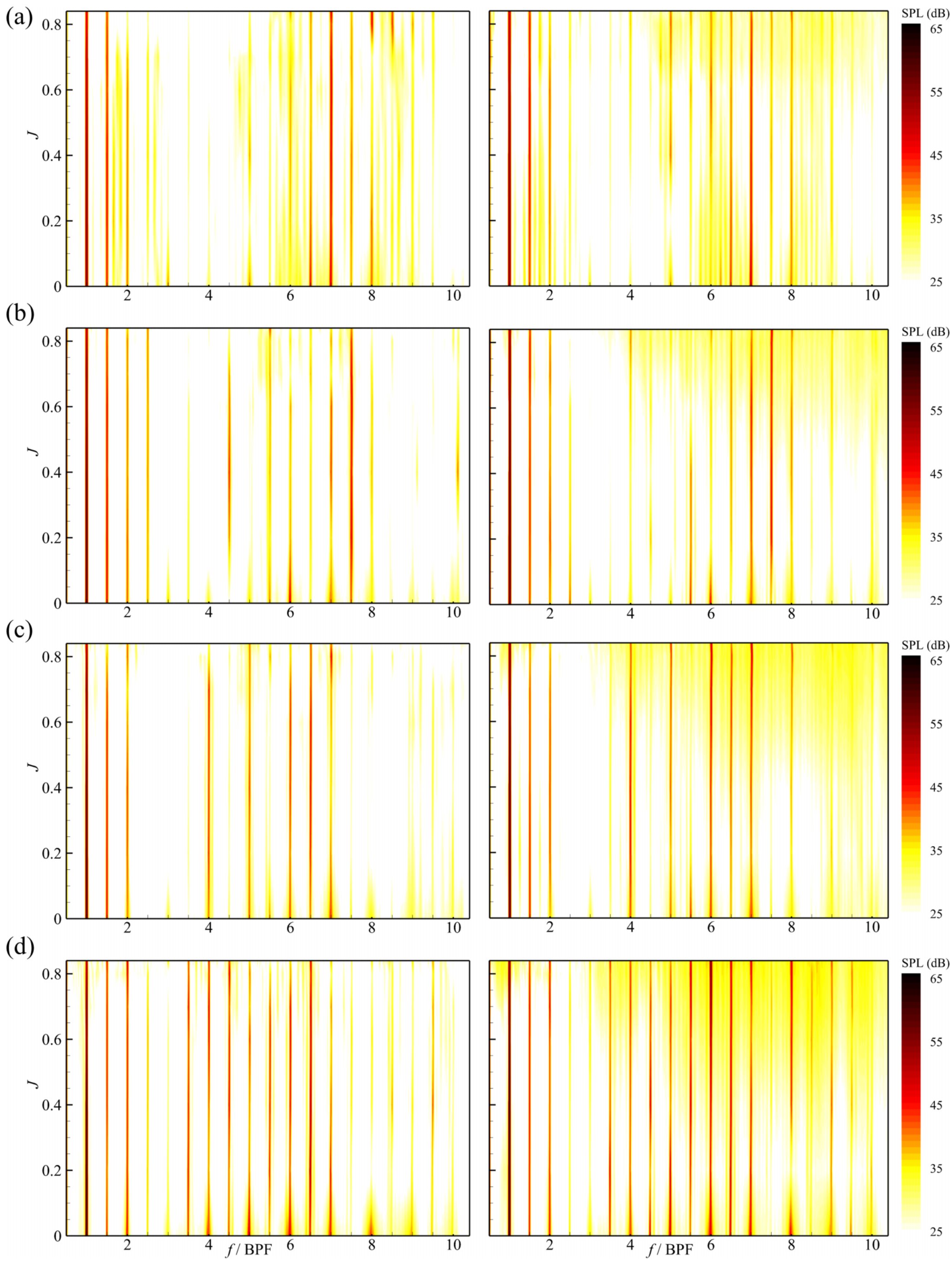

FIG. 16. SPL contours (at $\theta = 90^{\circ}$) of the first 10 BPF harmonics for (a) 90 RPS, (b) 100 RPS, (c) 110 RPS, and (d) 120 RPS. Left column: clean flow; right column: grid turbulence. The background noise was removed from the contours.

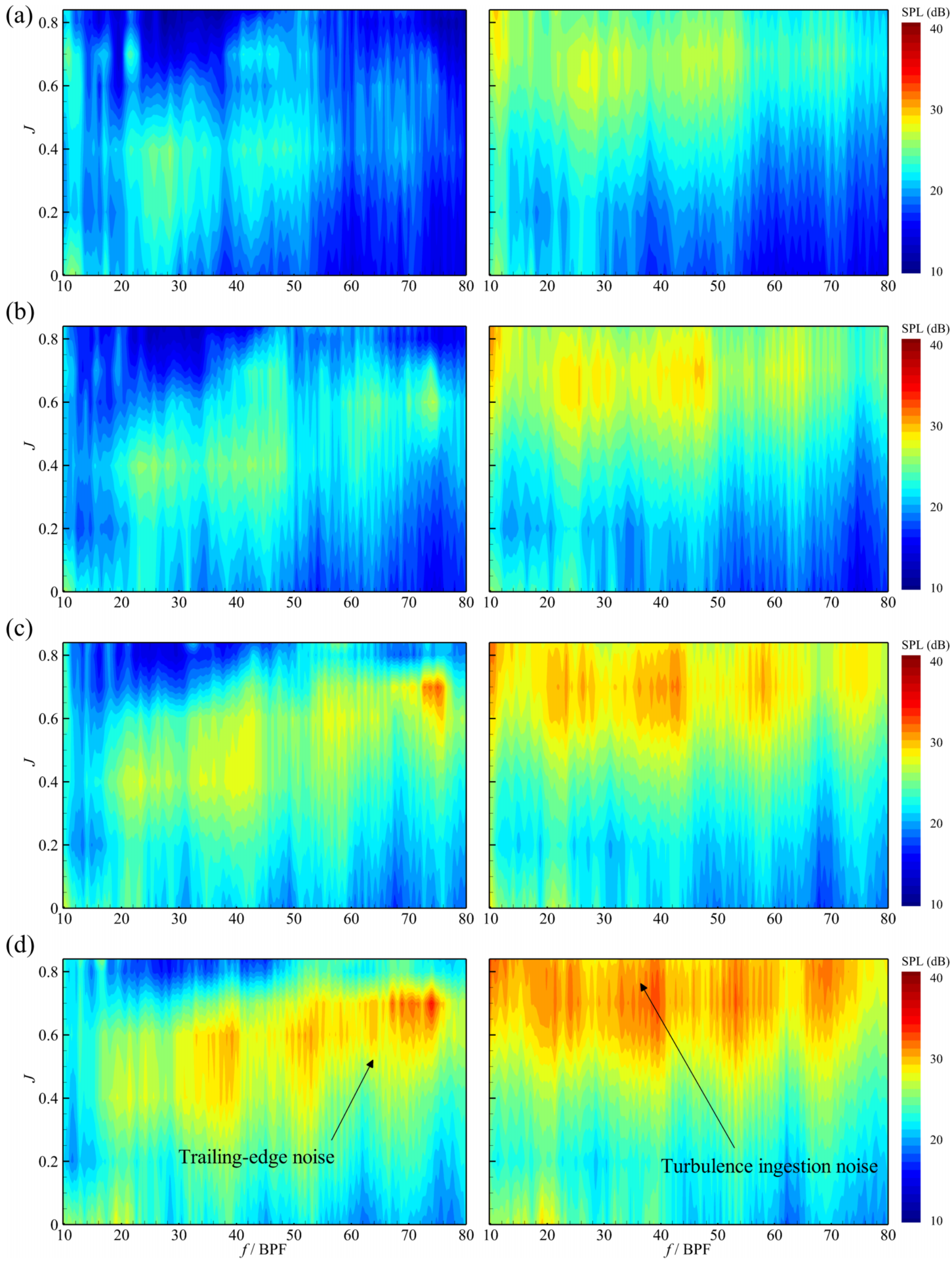

FIG. 17. SPL contours (at $\theta = 90^{\circ}$) of rotor broadband noise. Other setups are the same as those in Fig. 16.

2. Noise directivity

To demonstrate noise directivity under different thrusting conditions, we present results obtained under high-thrusting ($J = 0.2$), low-thrusting ($J = 0.7$), and zero-thrusting ($J = 0.84$) in Figs. 18

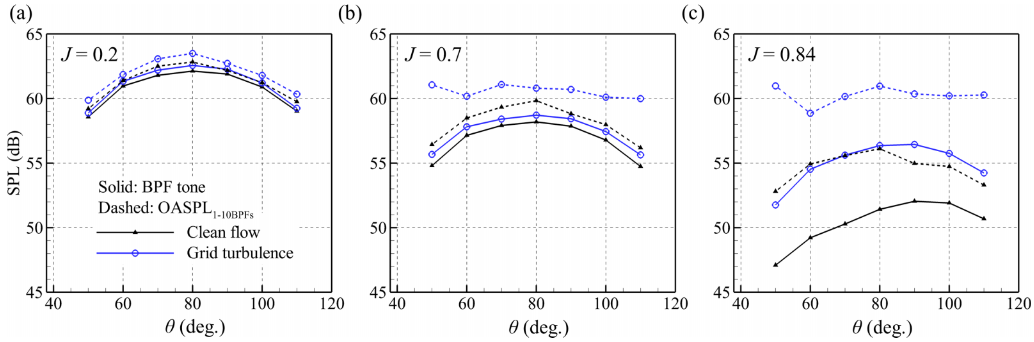

FIG. 18. Directivities comparison for tonal noise under various thrusting conditions. The rotor was rotating at 120 RPS.

and 19. For tonal noise, the primary tone at the BPF and the overall sound pressure level (OASPL) of the first 10 BPF harmonics are considered.

At $J = 0.2$ and 0.7, the BPF tone is most significant near the rotational plane ($\theta = 90^\circ$). Interestingly, the BPF shows an increasing pattern towards upstream at zero-thrusting conditions ($J = 0.84$), for both clean flow and grid turbulence. In terms of noise level, the primary tone is mainly attributed to the rotor steady loading [11]. Thus, the BPF tone decreases with J, as the increasing axial flow velocity reduces the averaged blade loadings (Fig. 13). Meanwhile, the BPF tone under grid turbulence is slightly higher at $J = 0.2$ and 0.7, and the difference in noise level is notably larger at $J = 0.84$, which agrees with the aerodynamic force measurements.

The OASPL of the tonal noise components is computed by summing the acoustic spectral power of the first 10 blade-passing frequencies, which is denoted by $\mathrm{OASPL}_{1-10\mathrm{BPFs}}$. According to the tonal noise contours in Fig. 16, high-order BPF harmonics could be amplified under higher advance ratios. Therefore, $\mathrm{OASPL}_{1-10\mathrm{BPFs}}$ can provide a more comprehensive profile of the tonal components in terms of level and directivity under different flow conditions. At the high-thrusting condition ($J = 0.2$), $\mathrm{OASPL}_{1-10\mathrm{BPFs}}$ can maintain the shape of the noise directivity as the BPF tone for both flow conditions. The noise difference compared to the BPF tone is within 1 dB. At the low-thrusting condition ($J = 0.7$), the noise directivity under clean flow can be retained, and the $\mathrm{OASPL}_{1-10\mathrm{BPFs}}$ is approximately 2 dB higher than the BPF tone. However, the directivity of tonal components changes significantly under grid turbulence at $J = 0.7$. The shape of the noise directivity becomes flatter compared to the BPF tone, and the discrepancies between all observers are within 1 dB. The noise difference can be up to 5 dB at $\theta = 50^\circ$ compared to the BPF

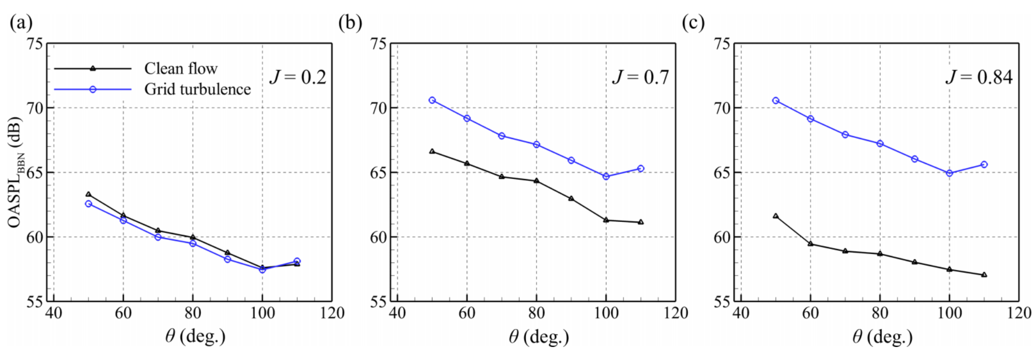

FIG. 19. Directivities comparison for the OASPL of broadband noise (from 1000 to 20 000 Hz) under various thrusting conditions. The rotor was rotating at 120 RPS.

tone. The results at $J = 0.7$ suggest that high-order BPF harmonics can be amplified by ingested turbulence under low-thrusting conditions, and this effect is more significant in both the upstream and downstream directions. At $J = 0.84$, this effect is even more significant for both flow conditions. Notably, for the grid turbulence case, the difference between $\mathrm{OASPL}_{1-10\mathrm{BPFs}}$ and the BPF tone can reach 10 dB, indicating significant amplifications of high-order harmonics caused by turbulence ingestion.

The effect of turbulence ingestion on broadband noise is also assessed by extracting broadband contents from narrowband spectra using a local regression method [9,15,38]. We estimate the overall sound pressure level of broadband noise, $\mathrm{OASPL}_{\mathrm{BBN}}$, by integrating the acoustic energy from 1000 to 20 000 Hz, and the directivities under various thrusting conditions are shown in Fig. 19. In general, the directivity for broadband noise shows a nearly monotonic increasing pattern towards downstream for all thrusting conditions. The effect of turbulence ingestion is negligible at $J = 0.2$, where the blade loadings are quite similar for clean flow and grid turbulence. At $J = 0.7$, the turbulence ingestion yields a considerable increase of 4–5 dB in the broadband noise. Particularly, the augmentation of broadband level is slightly greater at upstream locations. At a more extreme condition of $J = 0.84$, where the rotor can maintain only a negligible amount of thrust, the broadband noise level of the grid turbulence case is nearly identical to that of $J = 0.7$, while the broadband level of clean flow decreases by another 5 dB. The drop in noise level is likely due to the thrusting loss of the rotor at $J = 0.84$.

3. Dependence of the broadband noise of rotor-turbulence interaction on the flow and rotating speeds

In practical applications, the dependence of sound emission on key influential parameters is favorable for rapid estimation of noise. Furthermore, the considered parameters should be able to reveal the physics of sound generation. For the turbulence ingestion noise, we mainly consider the coherent structures in turbulent flows and the effect of blade rotation. In this section, we study the dependence of broadband noise under various turbulent flows based on the experimental data.

As a classical model for airfoil-turbulence interaction noise, the Sears theory [19] provides a relationship for estimating the unsteady lift of a thin airfoil and the upwash velocity encountered by the airfoil. A Mach number scaling law based on the Sears theory is derived for a rotor ingesting turbulent flows [56], suggesting that the rotor acoustic power spectrum $\Phi_{pp}(f)$ can be scaled with $M_\infty^2 M_c^4$, where M_∞ and M_c are the Mach number based on convection velocity and freestream velocity, respectively.

In this section, the scaling law of $M_\infty^2 M_c^4$ is implemented to study the broadband noise due to the interaction of turbulence and rotor under various working conditions. The convection velocity at blade tip is estimated as $U_c = \sqrt{(\Omega R)^2 + U_\infty^2}$, since the noise generation is significant in the blade tip region. M_∞ is also considered based on U_∞ as the upwash velocity is dominated by the oncoming turbulent flow. The frequency f is also scaled with $U_\infty R$ in the scaling analysis.

In Fig. 20, the rotor acoustic power spectra for various flow conditions are compared at different observer angles with the $M_\infty^2 M_c^4$ and $f \sim U_\infty R$ scalings. The unscaled noise spectra are also given. Measurement results obtained from various rotational speeds and advance ratios are plotted in the same figure. In general, results with the Mach number and frequency scaling can get a reasonable agreement for fR/U_∞ ranges from 20 to 80, indicating the dominant frequency range of turbulence ingestion. Within the above-mentioned range, the turbulence ingestion broadband noise exhibits a monotonically increasing trend, and the noise level can be well scaled with a maximum deviation less than 2 dB.

V. CONCLUSIONS

In this work, the aeroacoustic effect of a rotor ingesting grid turbulence is studied. A passive turbulence grid was installed in the jet exit of an anechoic wind tunnel to produce turbulent flows. The flow properties were examined by the hot-wire anemometry at multiple downstream locations of

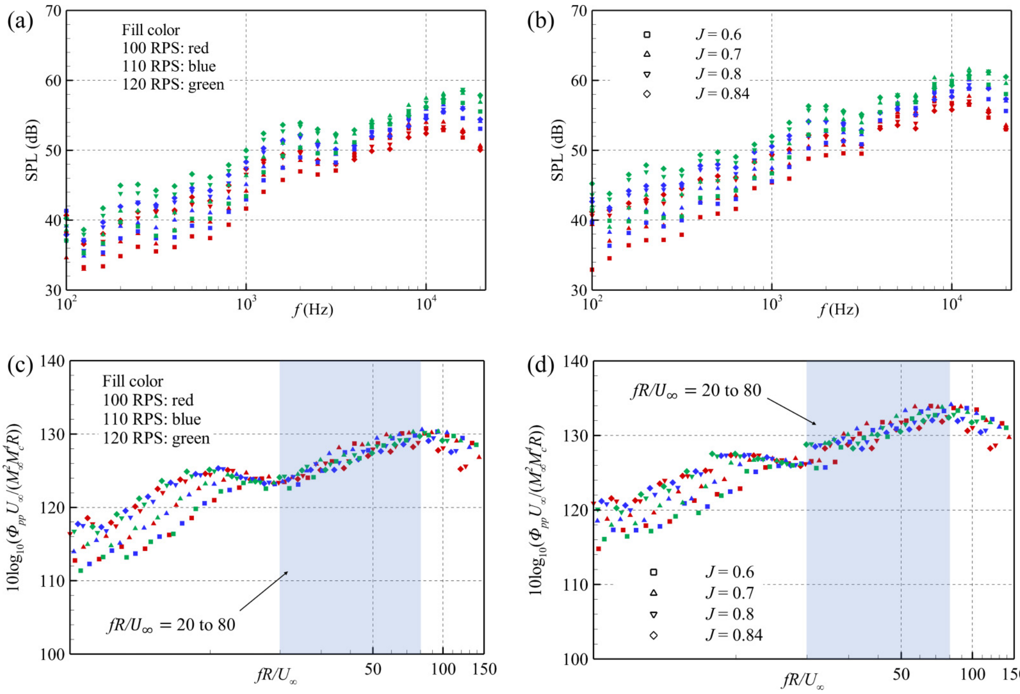

FIG. 20. 1/3 octave band spectra comparison: unscaled results at (a) $\theta = 90^\circ$ and (b) $\theta = 60^\circ$; scaled results with the $M_\infty^2 M_c^4$ vs U_∞/R scaling at (c) $\theta = 90^\circ$ and (d) $\theta = 60^\circ$.

the grid. Results show that the turbulence intensity decays with the streamwise locations, following a power law of $-5/7$. The power spectral properties of the grid turbulence were also assessed, which show a good agreement with the von Kármán turbulence spectrum in the inertial subrange, suggesting that the grid turbulence can be considered nearly isotropic in the streamwise direction. The aerodynamic coefficients of the rotor with respect to the advance ratio J collapse well for all the tested rotational speeds. The grid turbulence can significantly affect the rotor noise for both spectral characteristics and directivity patterns. The effect of turbulence ingestion is more significant in the directions normal to the rotational plane for both tonal and broadband noise. The high-order BPF harmonics can be amplified considerably by ingested turbulence, especially at higher advance ratios. As for the broadband noise, the turbulent flows mainly affect the broadband contents at $fR/U_\infty = 20$–80. The broadband noise can be scaled by the Mach number scaling of $M_\infty^2 M_c^4$ in this range.

ACKNOWLEDGMENT

This work is supported by the Hong Kong Research Grant Council (RGC 16206422) and the National Natural Science Foundation of China (NSFC 11972029).

APPENDIX A: ESTIMATION OF THE STREAMTUBE RADIUS AND SHEAR LAYER THICKNESS AT THE ROTOR PLANE

One concern in this study is that the rotor disk could effectively pull in the shear layer generated downstream of the jet nozzle if the rotor thrust is relatively high. A sketch of the problem statement is shown in Fig. 21. As shown in Fig. 21(a), the freestream is pulled into the rotor disk and accelerated. Consequently, the thrusting of the rotor causes the streamtube contraction. The streamtube upstream

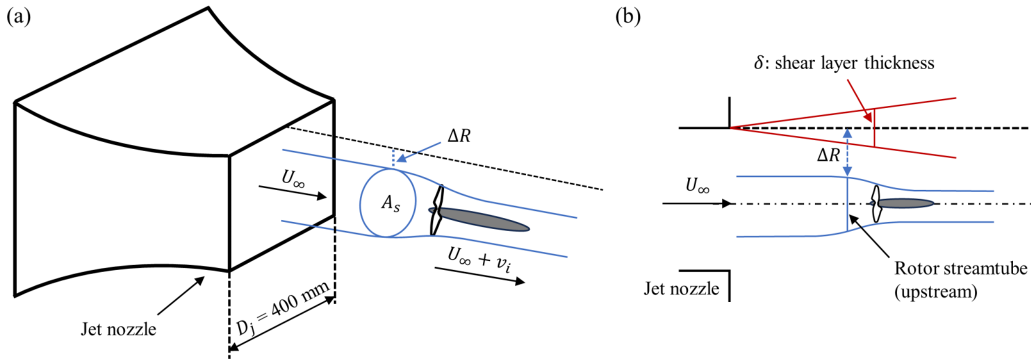

FIG. 21. Problem statement: (a) the rotor streamtube contraction in the presence of an open-jet wind tunnel; (b) schematic top view of the open-jet shear layer expansion downstream of the jet nozzle.

of the rotor is the location where the streamtube is closest to the shear layer. The distance between the rotor streamtube and the tunnel wall is defined as ΔR. Also, Fig. 21(b) presents the schematic of the expanding shear layer and the rotor streamtube. The shear layer thickness at the rotor plane is denoted by δ, which is assumed to be symmetrical about the tunnel wall. Thus, the potential entrainment of the shear layer into the rotor can be assessed by comparing ΔR and $\delta/2$.

An actuator disk analysis [57] is conducted to estimate the radius of the rotor streamtube. The rotor thrust T can be obtained by

$$T = 2\rho A_T v_i (U_\infty + v_i), \tag{A1}$$

where v_i is the induced velocity at the disk plane and $A_T = A - A_{\text{body}}$ is the total thrusting area. Thus, v_i can be solved as

$$v_i = \frac{-U_\infty + \sqrt{U_\infty^2 + 2T/(\rho A_T)}}{2}. \tag{A2}$$

Then, the mass continuity equation can be approximated by

$$A_s U_\infty = A_T (U_\infty + v_i), \tag{A3}$$

where A_s is the area of the streamtube upstream of the rotor, which contracts to the rotor plane as the flow is accelerated by the rotor.

By substituting Eq. (A2) into Eq. (A3), it yields

$$A_s U_\infty = A_T \left(\frac{U_\infty}{2} + \frac{1}{2}\sqrt{U_\infty^2 + \frac{2T}{\rho A_T}} \right), \tag{A4}$$

and it can be further written as

$$\frac{A_s}{A_T} = \frac{1}{2} + \frac{1}{2}\sqrt{1 + \frac{C_T D^2 \pi^3}{2 A_T J^2}}, \tag{A5}$$

which indicates the contraction of the slipstream caused by the addition of momentum at the rotor disk. This ratio approaches 1 as C_T approaches 0.

The distance between the rotor streamtube and the tunnel wall is given by

$$\Delta R = \frac{D_j}{2} - R_s, \tag{A6}$$

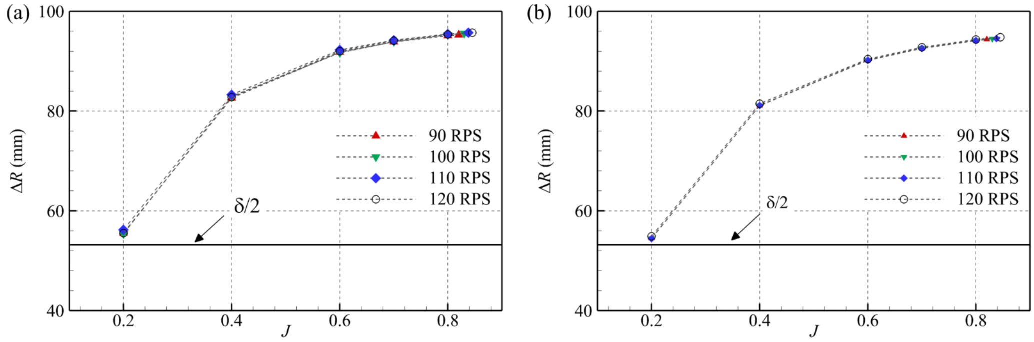

FIG. 22. Estimated results of potential core radius R_o at various working conditions under (a) clean flow and (b) grid turbulence.

where

$$R_s = \sqrt{\frac{A_s}{\pi}}, \tag{A7}$$

and D_j is the jet diameter (400 mm for current configuration).

In this work, ΔR can be computed by Eqs. (A5) and (22) by using the measured C_T values as input. The estimated ΔR values at various advance ratios and rotation rates are plotted for both clean flow and grid turbulence cases. As demonstrated in Fig. 22, the data measured at different rotation rates can obtain good agreement for both flow conditions. The value of ΔR increases with J due to decreasing rotor thrust coefficient.

The open-jet shear layer thickness downstream the nozzle can be approximated according to Ref. [58]:

$$\delta = \frac{6}{\sqrt{2\pi}} \frac{X}{\sigma}, \tag{A8}$$

where X is the streamwise location downstream of the nozzle as indicated in Fig. 1, and σ is an empirical constant. For the current measurement setup, the value of σ follows Ref. [58] as 9, as the nozzle dimensions are similar.

The value of $\delta/2$ is plotted as the solid black lines in Fig. 22. For all the present measurements, the values of ΔR do not exceed $\delta/2$. Thus, we can ensure that none of the turbulence ingestion is due to the entrainment of the tunnel open-jet shear layer for the current test configuration.

[1] R. Goyal, C. Reiche, C. Fernando, J. Serrao, S. Kimmel, A. Cohen, and S. Shaheen, Urban air mobility (UAM) market study, NASA Technical Report HQ-E-DAATN65181 (2018), https://ntrs.nasa.gov/citations/20190001472.

[2] S. Rajendran and S. Srinivas, Air taxi service for urban mobility: A critical review of recent developments, future challenges, and opportunities, Transp. Res. Pt. E: Logist. Transp. Rev. **143**, 102090 (2020).

[3] H. H. Hubbard, *Aeroacoustics of Flight Vehicles: Theory and Practice* (National Aeronautics and Space Administration, Office of Management, Scientific and Technical Information Program, 1991), Vol. 1.

[4] S. Zhong, P. Zhou, W. Chen, H. Jiang, H. Wu, and X. Zhang, An investigation of rotor aeroacoustics with unsteady motions and uncertainty factors, J. Fluid Mech. **956**, A16 (2023).

[5] J. E. Ffowcs Williams and D. L. Hawkings, Sound generation by turbulence and surfaces in arbitrary motion, Philos. Trans. R. Soc. London, A **264**, 321 (1969).

[6] T. F. Brooks, J. R. Jolly Jr, and M. A. Marcolini, Helicopter main-rotor noise: Determination of source contributions using scaled model data, NASA Technical Paper 2825 (1988), https://ntrs.nasa.gov/citations/19880017523.

[7] J. Brandt and M. Selig, Propeller performance data at low Reynolds numbers, AIAA Paper 2011-1255 (2011), doi: 10.2514/6.2011-1255.

[8] N. S. Zawodny, D. D. Boyd Jr, and C. L. Burley, Acoustic characterization and prediction of representative, small-scale rotary-wing unmanned aircraft system components, AHS Paper 20160009054 (2016), https://ntrs.nasa.gov/citations/20160009054.

[9] R. J. Fattah, W. Chen, H. Wu, Y. Wu, and X. Zhang, Noise measurements of generic small-scale propellers, AIAA Paper 2019-2498 (2019), doi: 10.2514/6.2019-2498.

[10] C. E. Tinney and J. Sirohi, Multirotor drone noise at static thrust, AIAA J. **56**, 2816 (2018).

[11] S. Zhong, P. Zhou, R. Fattah, and X. Zhang, A revisit of the tonal noise of small rotors, Proc. R. Soc. A **476**, 20200491 (2020).

[12] H. Bu, H. Wu, C. Bertin, Y. Fang, and S. Zhong, Aerodynamic and acoustic measurements of dual small-scale propellers, J. Sound Vib. **511**, 116330 (2021).

[13] W. Chen, Z. Yang, B. Peng, and X. Huang, On trailing edge noise from propellers with interactions to shear layers, J. Sound Vib. **495**, 115901 (2021).

[14] E. Grande, G. Romani, D. Ragni, F. Avallone, and D. Casalino, Aeroacoustic investigation of a propeller operating at low Reynolds numbers, AIAA J. **60**, 860 (2021).

[15] H. Wu, W. Chen, H. Jiang, S. Zhong, and X. Zhang, Experimental investigation of the effect of sectional airfoil profile deviation on propeller noise, Phys. Fluids **35**, 027104 (2023).

[16] A. R. Jones, O. Cetiner, and M. J. Smith, Physics and modeling of large flow disturbances: Discrete gust encounters for modern air vehicles, Annu. Rev. Fluid Mech. **54**, 469 (2022).

[17] C. W. Murray and D. Anderson, A CFD-based procedure for airspace integration of small unmanned aircraft within congested areas, Int. J. Micro Air Veh. **9**, 235 (2017).

[18] M. Sevik, Sound radiation from a subsonic rotor subjected to turbulence, in *Fluid Mechanics, Acoustics, and Design of Turbomachinery* (Pt. 2, NASA SP-304, 1974), pp. 493–512.

[19] W. R. Sears, Some aspects of non-stationary airfoil theory and its practical application, J. Aeronaut. Sci. **8**, 104 (1941).

[20] J. P. Wojno, T. J. Mueller, and W. K. Blake, Turbulence ingestion noise, Part 1: Experimental characterization of grid-generated turbulence, AIAA J. **40**, 16 (2002).

[21] J. P. Wojno, T. J. Mueller, and W. K. Blake, Turbulence ingestion noise, Part 2: Rotor aeroacoustic response to grid-generated turbulence, AIAA J. **40**, 26 (2002).

[22] J. Wu, J. Yangzhou, Z. Ma, and X. Huang, Numerical study of rotor unsteady forces and noise due to ingestion of grid-generated turbulence, Phys. Fluids **35**, 015141 (2023).

[23] S. A. Glegg, W. Devenport, and N. Alexander, Broadband rotor noise predictions using a time domain approach, J. Sound Vib. **335**, 115 (2015).

[24] S. A. Glegg, A. Buono, J. Grant, F. Lachowski, W. J. Devenport, and W. N. Alexander, Sound radiation from a rotor partially immersed in a turbulent boundary layer, AIAA Paper 2015-2361 (2015), doi: 10.2514/6.2015-2361.

[25] W. N. Alexander, W. J. Devenport, and S. A. Glegg, Noise from a rotor ingesting a thick boundary layer and relation to measurements of ingested turbulence, J. Sound Vib. **409**, 227 (2017).

[26] H. H. Murray, W. J. Devenport, W. N. Alexander, S. A. Glegg, and D. Wisda, Aeroacoustics of a rotor ingesting a planar boundary layer at high thrust, J. Fluid Mech. **850**, 212 (2018).

[27] M. J. Hagen, G. K. Yamauchi, D. B. Signor, and M. Mosher, Measurements of atmospheric turbulence effects on tail rotor acoustics, NASA TM 108843 (1994), https://ntrs.nasa.gov/citations/19950005947.

[28] C. Nardari, D. Casalino, F. Polidoro, V. Coralic, P.-T. Lew, and J. Brodie, Numerical and experimental investigation of flow confinement effects on UAV rotor noise, AIAA Paper 2019-2497 (2019), doi: 10.2514/6.2019-2497.

[29] J. H. Stephenson, D. Weitsman, and N. S. Zawodny, Effects of flow recirculation on unmanned aircraft system (UAS) acoustic measurements in closed anechoic chambers, J. Acoust. Soc. Am. **145**, 1153 (2019).

[30] Y. Yauwenas, J. R. Fischer, D. Moreau, and C. J. Doolan, The effect of inflow disturbance on drone propeller noise, AIAA Paper 2019-2663 (2019), doi: 10.2514/6.2019-2663.

[31] N. S. Jamaluddin, A. Celik, K. Baskaran, D. Rezgui, and M. Azarpeyvand, Aeroacoustic performance of propellers in turbulent flow, AIAA Paper 2021-2188 (2021), doi: 10.2514/6.2021-2188.

[32] F. Petricelli, S. Palleja-Cabre, C. C. Paruchuri, P. Joseph, A. Karimian, S. Meloni, and R. Camussi, On the effect of inflow distortions of propeller noise, AIAA Paper 2022-2938 (2022), doi: 10.2514/6.2022-2938.

[33] S. T. Go, M. J. Kingan, Y. Wu, and R. N. Sharma, Experimental and numerical investigation of the sound field produced by a shrouded UAV propeller, Appl. Acoust. **211**, 109523 (2023).

[34] N. S. Jamaluddin, A. Celik, K. Baskaran, D. Rezgui, and M. Azarpeyvand, Experimental analysis of a propeller noise in turbulent flow, Phys. Fluids **35**, 075106 (2023).

[35] H. Jiang, H. Wu, W. Chen, P. Zhou, S. Zhong, X. Zhang, G. Zhou, and B. Chen, Toward high-efficiency low-noise propellers: A numerical and experimental study, Phys. Fluids **34**, 076116 (2022).

[36] S. A. Rizzi, D. L. Huff, D. D. Boyd, P. Bent, B. S. Henderson, K. A. Pascioni, D. C. Sargent, D. L. Josephson, M. Marsan, H. B. He *et al.*, Urban air mobility noise: Current practice, gaps, and recommendations, NASA/TP–2020-5007433 (2020), https://ntrs.nasa.gov/api/citations/20205007433/downloads/NASA-TP-2020-5007433.pdf.

[37] W. Yi, P. Zhou, Y. Fang, J. Guo, S. Zhong, X. Zhang, X. Huang, G. Zhou, and B. Chen, Design and characterization of a multifunctional low-speed anechoic wind tunnel at HKUST, Aerosp. Sci. Technol. **115**, 106814 (2021).

[38] H. Wu, W. Chen, R. Fattah, Y. Fang, S. Zhong, and X. Zhang, A rotor blade aeroacoustics test platform at HKUST, INTER-NOISE and NOISE-CON Congress and Conference Proceedings **261**, 2476 (2020), https://www.ingentaconnect.com/contentone/ince/incecp/2020/00000261/00000004/art00052.

[39] L. Bowen, A. Celik, M. Azarpeyvand, and C. R. I. da Silva, Grid generated turbulence for aeroacoustic facility, AIAA J. **60**, 1833 (2022).

[40] P. Welch, The use of fast Fourier transform for the estimation of power spectra: a method based on time averaging over short, modified periodograms, IEEE Trans. Audio Electroacoust. **15**, 70 (1967).

[41] F. Frenkiel, The decay of isotropic turbulence, J. Appl. Mech. **15**, 311 (1948).

[42] P. Roach, The generation of nearly isotropic turbulence by means of grids, Int. J. Heat Fluid Flow **8**, 82 (1987).

[43] T. von Kármán, Progress in the statistical theory of turbulence, Proc. Natl. Acad. Sci. (USA) **34**, 530 (1948).

[44] H. S. Kang, S. Chester, and C. Meneveau, Decaying turbulence in an active-grid-generated flow and comparisons with large-eddy simulation, J. Fluid Mech. **480**, 129 (2003).

[45] S. Zheng, P. J. K. Bruce, C. Cuvier, J.-M. Foucaut, J. M. R. Graham, and J. C. Vassilicos, Nonequilibrium dissipation scaling in large Reynolds number turbulence generated by rectangular fractal grids, Phys. Rev. Fluids **6**, 054613 (2021).

[46] M. Gad-El-Hak and S. Corrsin, Measurements of the nearly isotropic turbulence behind a uniform jet grid, J. Fluid Mech. **62**, 115 (1974).

[47] G. K. Batchelor and A. A. Townsend, Decay of isotropic turbulence in the initial period, Proc. R. Soc. London A **193**, 539 (1948).

[48] G. K. Batchelor and A. A. Townsend, Decay of turbulence in the final period, Proc. R. Soc. London A **194**, 527 (1948).

[49] J. Bennett and S. Corrsin, Small Reynolds number nearly isotropic turbulence in a straight duct and a contraction, Phys. Fluids **21**, 2129 (1978).

[50] J. C. Isaza, R. Salazar, and Z. Warhaft, On grid-generated turbulence in the near-and far field regions, J. Fluid Mech. **753**, 402 (2014).

[51] Jayesh and Z. Warhaft, Probability distribution, conditional dissipation, and transport of passive temperature fluctuations in grid-generated turbulence, Phys. Fluids **4**, 2292 (1992).

[52] Jayesh and Z. Warhaft, Probability distribution of a passive scalar in grid-generated turbulence, Phys. Rev. Lett. **67**, 3503 (1991).

[53] Y. Zheng, K. Nakamura, K. Nagata, and T. Watanabe, Unsteady dissipation scaling in static-and active-grid turbulence, J. Fluid Mech. **956**, A20 (2023).

[54] G. J. Leishman, *Principles of Helicopter Aerodynamics* (Cambridge University Press, New York, 2006).

[55] H. Wu, H. Jiang, P. Zhou, S. Zhong, X. Zhang, G. Zhou, and B. Chen, On identifying the deterministic components of propeller noise, Aerosp. Sci. Technol. **130**, 107948 (2022).

[56] J. Wang, K. Wang, and M. Wang, Computational prediction and analysis of rotor noise generation in a turbulent wake, J. Fluid Mech. **908**, A19 (2021).

[57] P. J. W. Block, Operational evaluation of a propeller test stand in the quiet flow facility at Langley Research Center, NASA-TM-84523 (1982), https://ntrs.nasa.gov/citations/19820025273.

[58] Z. Sulaiman, Effect of open-jet shear layers on aeroacoustic wind tunnel measurements, M.Sc. thesis, Delft University of Technology (2011), https://repository.tudelft.nl/islandora/object/uuid%3Afbb5d74e-4ae5-436d-836c-f8007184dba1.